THESIS FOR THE DEGREE OF LICENTIATE OF ENGINEERING

The dust doesn't settle in merger galaxy II Zw 096

GUSTAV OLANDER

CHALMERS
UNIVERSITY OF TECHNOLOGY

Department of Space, Earth and Environment
Chalmers University of Technology
Gothenburg, Sweden, 2025

The dust doesn't settle in merger galaxy II Zw 096

GUSTAV OLANDER

Department of Space, Earth and Environment
Chalmers University of Technology
SE-412 96 Gothenburg,
Sweden
Telephone: +46 (0)31 772 1000

Cover image:
James Webb Space Telescope image of merger luminous infrared galaxy II Zw 096.
Credit: ESA/Webb, NASA & CSA, L. Armus, A. Evans Printed by Chalmers

Reproservice
Gothenburg, Sweden, 2025

Abstract

Understanding galaxy formation and evolution is one of the central goals of modern astronomy. Investigating the life cycle and properties of the components within galaxies can provide valuable insights into these processes. The interstellar medium consists of gas and dust, with the latter being 1% of the interstellar medium by mass. However, cosmic dust grains, which are small solid particles, significantly affect physical and chemical processes and thus play an important role in galaxy evolution. Previous studies of dust have shown how the physical environment triggers a variation in dust properties such as size distribution and grain composition. These properties can be traced by observing emission from stochastically heated nanograins in the mid-infrared using observatories such as the *James Webb* Space Telescope *(JWST)*.

This thesis provides a summary of how dust properties, with a focus on nanograins, vary and how they link to galaxy evolution in our nearby Universe, in particular in the dusty (Ultra-)Luminous InfraRed Galaxies (LIRGs and ULIRGs). Also described is the workings of *JWST* and the spectral decomposition tool CAFE (Continuum And Feature Extraction tool) used in the analysis in the included paper.

Using *JWST* Near Infrared Spectrograph (NIRSpec) and Mid-InfraRed Instrument (MIRI) spectroscopic data from nearby LIRG II Zw 096 it could be concluded that the average dust grain size vary across the field of view. The ratio of aromatic (ring structured carbon chains) to aliphatic (open carbon chains) compounds in the dust grains was also shown to vary, though to a lesser extent. A larger average dust grain size was observed towards more extreme environments such as towards a proposed obscured AGN. This is also where the aliphatic compounds seem to be more efficiently destroyed.

The thesis provide new insights on how dust properties vary with the environment where it is found, in particular in the extreme environments in LIRGs. Further investigation of how dust properties vary in the most extreme environments in our Universe, the Compact Obscured Nuclei (CON) is of high importance to further understand galaxy evolution and how dust fit into the puzzle. Such targets include IC 860 and NGC 4418, which are of focus for future work.

Keywords: Galaxies: interactions – galaxies: ISM – infrared: galaxies – ISM: dust, extinction – techniques: spectroscopic.

List of Publications

This thesis is based on the following publications:

[A] **Olander, G.**, Schirmer, T., Aalto, S., Knudsen, K. K., Vlemmings, W., Nyman, G., Sameera W. M. C., del Palacio S., Wethers, C., Diaz-Santos, T., Lai, T. S.-Y., "*Carbonaceous Dust Processing in the Merger Galaxy II Zw 096: High-Resolution PAH Diagnostics with JWST*". To be submitted to Astronomy & Astrophysics.

Acknowledgments

I would like to sincerely thank my supervisors, Thiébaut Schirmer and Susanne Aalto, for their support. Thank you, Thiébaut, for always making sure I was on the right track and for sharing your invaluable expertise and knowledge. Thank you, Susanne, for providing insight, guidance, and for helping me stay grounded and keep things in perspective.

I would also like to thank my examiner, Kirsten Kraiberg Knudsen, for insightful comments and constructive feedback that helped improve this thesis.

I am grateful to all members of the Cosmic Dust research group at Chalmers University of Technology and the University of Gothenburg. I am equally thankful to the Knut & Alice Wallenberg Foundation for supporting the fascinating and important research carried out by the Cosmic Dust group — your support makes our work possible.

Lastly, I would like to thank my family for embracing my passion for astronomy and for cheering me on every step of the way.

Contents

List of Figures

CHAPTER 1

Introduction

1.1 Some history

In 1785, William Herschel proposed our sun to be situated in a disc-like distribution of stars and started a journey towards new understandings of the Universe we live in (Herschel, 1785). A hundred years later, Kapteyn and von Rhijn mapped stars based on magnitude, color and motion and concluded that the stellar system of our Sun was shaped as a thin oblate with the Sun in the center (Kapteyn and Rhijn, 1920). A few years later, Kapteyn could also draw the conclusion that the system was not stationary (Kapteyn, 1922). Kapteyn's work on the structure of our Universe became known as the "Kapteyn's Universe". Around the same time, Harlow Shapley proposed a different model after observing that most large star-clusters were found around the Sagittarius constellation (Shapley, 1923). Shapley suggested that this is the actual center of our Galaxy, which still was thought to be the whole Universe. His proposition was a stellar disc with a bulge in the middle, surrounded by the large stellar clusters. Although much has been added, this model remains fundamentally correct today.

In 1922, Erwin Hubble demonstrated that some nebulae were not located

in our galaxy, but rather they were individual stellar systems (Hubble, 1925). By doing so, he settled the "great debate" of astronomy and our Milky Way galaxy was now known to be just a galaxy among many in the vast Universe. This discovery established the field of extragalactic astronomy.

1.2 Galaxies and dust

Since those days, galaxies of all shapes, sizes and distances from us have been found. Observing and mapping the components of galaxies and understanding the physics governing their processes and properties is key to understanding the Universe we live in. Proposed models of how the interstellar medium (ISM) cycles through cloud collapses into stars, which eventually age and die and feed material back into the ISM, are always in need of refinement to further our understanding. Dust is a component of the ISM with sizes spanning from less than a nanometer to micrometers in size. Although constituting only up to 1% of the mass of the ISM, dust significantly affects the physics of our Universe. Interstellar dust serves essential functions in the ISM through multiple physical mechanisms on grain surfaces, such as gas heating via the photoelectric effect (e.g. Bakes et al., 1994; Weingartner et al., 2001) and gas cooling through grain-gas collisions (Burke et al., 1983). As a chemical catalyst, dust facilitates surface reactions and is fundamental to ISM chemistry (e.g. Hollenbach et al., 1971; Bron et al., 2014). Dust also transforms stellar ultra violet (UV) to visible light into infrared (IR) and millimeter wavelengths, with efficiency determined by grain properties (e.g. Draine, 2003; Compiègne et al., 2011). The effectiveness of these mechanisms depends critically on dust characteristics including grain size, composition and morphology. Consequently, determining dust properties is essential for comprehending the various processes occurring in the ISM and therefore, in galaxies.

1.3 Thesis outline

The aim of this thesis is to gain an understanding of the properties of dust in galaxies that are undergoing a major merger event where the star formation activity is increased. While dust initially was identified due to obscuration, which gave insights to a number of physical properties, the emission from dust can be used as a diagnostic tool to understand the environments where

it is found. Luminous InfraRed Galaxies (LIRGs) are dusty objects emitting strongly in the infrared, thereby providing excellent laboratories to study dust properties and dust evolution. This thesis focuses on emission from stochastically heated carbonaceous nano-grains in the nearby LIRG II Zw 096 using the *James Webb* Space Telescope *(JWST)* with the aim of understanding how dust properties evolve in dense and highly radiated regions. II Zw 096 is a galaxy merger known for its luminous starburst regions and complicated structure, making it a particularly interesting target for such studies.

Furthermore, the thesis describes the workings of *JWST* and data reduction methods of its observational data products as well as adoption and expansion of the Continuum and Feature Extraction tool (CAFE). CAFE is a Python based spectral decomposition tool developed for *JWST* observations and has been the central data analysis tool in the included paper. Chapter 2 provides a brief background to the world of galaxies and in particular dust-obscured galactic nuclei. Chapter 3 presents an introduction to dust in our Universe with focus on the carbonaceous dust features in the mid IR. Chapter 4 presents the *JWST*, outlines its data reduction pipeline and data products, and introduces CAFE along with the additional functionality implemented. Chapter 5 presents a short summary of the included paper and the thesis concludes in Chapter 6 with a summary of the thesis and an outlook on possible future projects.

CHAPTER 2

Galaxies

From tradition, we classify galaxies as spiral or elliptical galaxies. The spiral galaxies are disc shaped galaxies with spiral structures, though the number of arms can vary. These galaxies harbor young stars, have active star formation and much gas and dust. Elliptical galaxies, on the other hand, have exhausted their reservoirs of gas and dust and have little to no star formation, therefore containing older stellar populations.

2.1 Galaxy classification

Galaxies are often classified following Hubble's classification scheme. In this system, galaxies in our Universe can be divided into three main categories; irregular- (Irr), elliptical- (E) and spiral (S and SB) galaxies. Hubble displayed these types in the famous "tuning fork diagram" (see Figure 2.1), where the elliptical galaxies to the left splits into spirals and barred spirals, with a transitional type where they meet.

The elliptical galaxies are identified by their lack of spiral structure and elliptical shape. These have little to no star formation and have a low mass-fraction of gas and dust, therefore consisting of an older population of stars

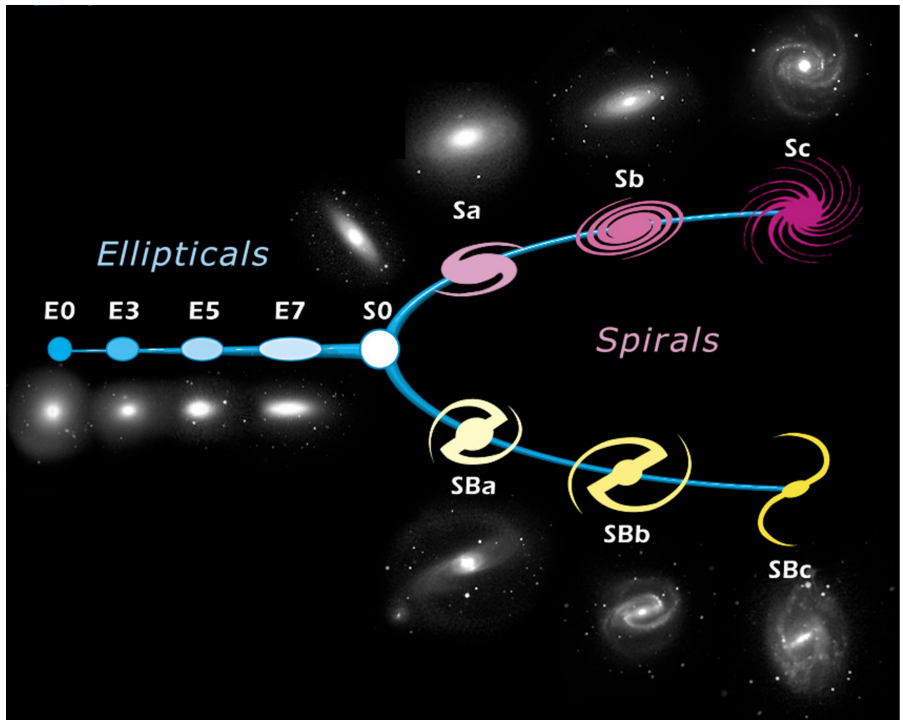

Figure 2.1: Edwin Hubble's galaxy classification scheme with the elliptical galaxies (E0-7) to the left and spiral galaxies to the right. The spiral galaxies are divided into regular spirals (Sa-c) and barred spirals (SBa-c). The elliptical and spiral galaxies meet in the lenticular galaxies (S0). *Image credit: NASA/ESA (Image labels edited by Gustav Olander) NASA/ESA, 1999*

with a red color. They are supported by random motion of the stars and hence have no velocity gradient. Subclasses of elliptical galaxies include; normal ellipticals (giant, intermediate and compact ellipticals, gE, E and cE respectively), dwarf ellipticals (dE), cD galaxies, blue compact dwarf galaxies (BCD) and dwarf spheroidal (dSph). The collective of elliptical galaxies spans through a range of properties, e.g. a mass- and luminosity range of over 10^6 (Choudhuri, 2010; Schneider, 2015).

The spiral galaxies are instead identified by the spiral structure and are subdivided into normal spirals (S) and barred spirals (Sb). The spirals are ordered according to their brightness ratio of the bulge and disk (a, b, c and d) (Schneider, 2015). The spiral arms vary in number, size and how tightly winded they are, ranging from minor arms to grand structure spirals and are probably formed by density waves (Binney et al., 2008). The spiral galaxies contains a significant amount of interstellar medium (ISM) and the structure is supported by approximately circular motions, orbiting the center of the galaxy. These galaxies have ongoing star formation due to the present ISM and is therefore more blue in color as compared to the elliptical. Barred spiral galaxies have similar morphology and additionally contain a bar extending from the central region. The bars can vary from prominent, galaxy dominating structures to weak oval distortions (Binney et al., 2008).

Between the elliptical and spiral galaxies are the lenticular galaxies (S0) containing a bulge and an enveloping region of brightness, sometimes appearing as a disk. In addition to the classifications in Figure 2.1 are the irregular galaxies identified by weak (Irr I) and no (Irr II) structure (Schneider, 2015).

Galaxy formation and growth

Observations of the cosmic background radiation (CMBR) from satellites like the Cosmic Background Explorer (COBE), Wilkinson Microwave Anisotropy Probe (WMAP) and Planck have revealed anisotropies of the CMB in the early Universe observed as tiny variations in the temperature of the CMB radiation at the scale of $\Delta T/T \sim 10^{-5}$ (e.g., Smoot et al., 1992; Hinshaw et al., 2012; Aghanim et al., 2018). The structures we see in the present Universe, have all evolved from these initial anisotropies. Overdense regions grow more slowly due to self-gravitation, resulting in amplified relative overdensities as the Universe evolves, causing large scale structure formation over time. The evolution of structures in our Universe can be observed by measuring the

star formation history, which peaks at redshift $z = 2$, known as cosmic noon. Cosmologically young galaxies are more blue than older galaxies at lower redshift, in which a shift to a more red color can be observed, which can be explained by the death of short lived massive stars. The CMB anisotropies and star formation history of our Universe tells us about the universal formation history. On a smaller scale, such as galaxies and cluster of galaxies, merger between galaxies and accretion plays a major role in the evolution.

Mergers

Collision of two or more galaxies constitutes one of the more violent physical processes in our Universe. Galaxy collisions disturb gas and dust morphology, triggering star formation and heating through shocks from supernova explosions and winds. However, stars rarely collide due to low stellar surface density. Close encounters often lead to mergers, especially for galaxies of comparable mass, but flybys and tidal interactions also occur. These are divided into major and minor mergers, in which the former is caused by galaxies of similar size colliding, and the latter when one galaxy is substantially larger. The collision leads to changes in the gravitational field which in the case of a major merger will result in a galaxy of vastly different morphology. However, in minor mergers, the larger galaxy remains relatively unchanged while the smaller galaxy is mostly or completely consumed. Understanding how mergers are involved in formation of large galaxies are of high importance, since it also tells us about the evolution of the Universe. The effects of collisions and mergers on the galaxies involved are also studied through modeling and simulation. Figure 2.2 shows an example of a major merger from N-body simulations (Binney et al., 2008; Schneider, 2015).

Accretion

The second main path for galaxy growth is accretion of gas. There are two modes of accretion; cold and hot accretion. In cold accretion, gas from the intergalactic medium (IGM) is accreted at low temperatures below the virial temperature ($T \sim 10^5$ K) and can add to the star formation on relative short timescales (Brooks et al., 2009). Gas is often provided to galaxies through large-scale filaments. This mode of accretion dominates at high redshift, in low-density regions at low redshift, and in low-mass galaxies. The hot mode

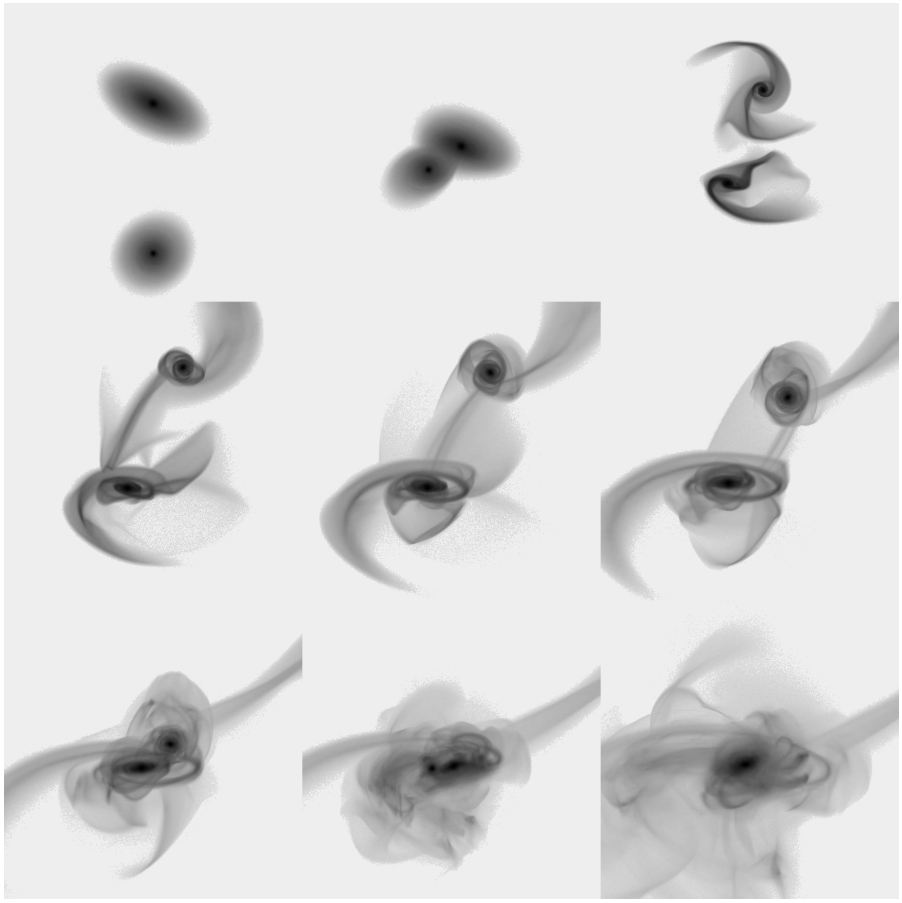

Figure 2.2: N-body simulation of a major merger between two galaxies, showing the formation of a single more massive galaxy. Figure from Binney et al., 2008

accretion describes hot gas (T$\sim 10^6$ K for a Milky way sized galaxy) that is being heated to virial temperatures before being cooled enough to add to the star formation. The hot mode dominates in high-mass systems such as galaxy clusters and is an important effect of mergers (Keres et al., 2004).

2.2 Active galaxies and active galactic nuclei

A galaxy with no star formation has a spectral energy distribution (SED) that can be approximated by a superposition of black body emission spectra of temperatures corresponding to the effective temperatures of the stars. Adding heated dust and starburst to the galaxy will extend the spectral range on both sides. However, some galaxies have much broader emission spectra and the excess emission seems to originate from highly spatially narrow regions within the galaxy, known as active galactic nucleus (AGN). The host galaxy is referred to as active galaxy and also present highly excited and broad emission lines indicating the highly energetic environment in the nucleus. The AGNs early appeared as unresolved point sources, indicating sizes as small as ~ 100 pc (Woltjer, 1959). The active galactic nucleus is often accompanied by jets of collimated gas being expelled from the small region, with radiation that can be used to constrain the properties of the emitting structure. The AGN can vary substantially over timescales as short as a day, indicating spatial extent of less than a light day (3×10^{15} cm). With characteristic luminosities of L $\sim 10^{47}$erg/s for AGNs this is not sufficient to be caused by nuclear energy. More probably, gravitational energy is the cause of the energy flux, leading to the conclusion that supermassive black holes (SMBHs) are the central engines.

2.3 Starburst galaxies

While our own galaxy has a star formation rate of $\sim 3M_\odot$/yr, there are galaxies with star formation rates over two orders of magnitude higher. These are the starburst galaxies and emits heavily in the far infrared (FIR) due to heated dust from the surrounding hot stars (Rieke, Lebofsky, et al., 1980; Weedman et al., 1981). Theories as to why these galaxies forms stars at such a high rates are believed to be interactions between galaxies, or mergers which ignite the star forming processes.

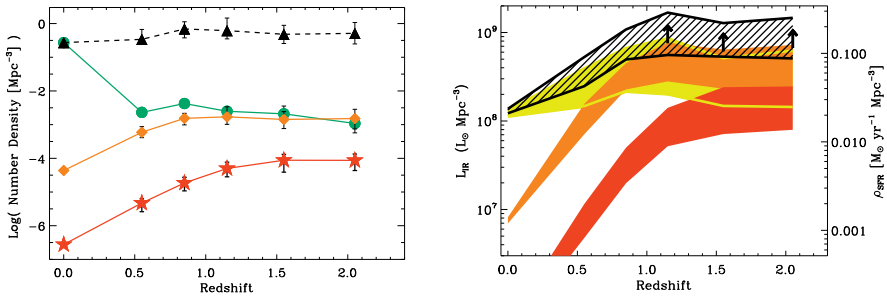

Figure 2.3: *(Left)* Evolution of (U)LIRGs over cosmic time. Black triangles correspond to "normal" galaxies with $10^7 L_\odot \leq L_{\rm IR} \leq 10^{11} L_\odot$, orange symbols represent LIRGs, and red symbols represent ULIRGs. Green circles are the number of galaxies above the 24 μm detection limit ($L_{\rm IR} \geq L_{\rm IR}^{\rm fluxlimit}$) in the survey by Magnelli, Elbaz, Chary, Dickinson, Le Borgne, et al., 2011. *(Right)* Evolution of total IR luminosity density (black) and relative contributions from "normal" galaxies (yellow), LIRGs (orange) and ULIRGs (red). Figure from Magnelli, Elbaz, Chary, Dickinson, Le Borgne, et al., 2011

2.4 (Ultra-) Luminous infrared galaxies

Galaxies that emits heavily in IR and FIR, with $10^{11} L_\odot < L_{8-1000\mu{\rm m}} < 10^{12} L_\odot$ are defined as Luminous Infrared Galaxies (LIRSs). Galaxies with IR luminosity $L_{8-1000\mu{\rm m}} > 10^{12} L_\odot$ are similarly defined as Ultra luminous infrared galaxies (ULRGs). This class of galaxies were defined as a result of the IR observations by the Infrared Astronomical Satellite (*IRAS*) (Neugebauer et al., 1984; Sanders and Mirabel, 1996; Sanders, Mazzarella, et al., 2003). Most of the bolometric infrared luminosity originates from warm dust heated by a nucleus consisting of either starburst, AGN or both. There is evidence of evolution of LIRGs and ULIRGs, with the incidence decreasing by factors of 40 and 100 for LIRGs and ULIRGs respectively from z$\sim$ 1 to $z = 0$ (Magnelli, Elbaz, Chary, Dickinson, Borgne, et al., 2009; Magnelli, Elbaz, Chary, Dickinson, Le Borgne, et al., 2011), see Figure 2.3. Additionally, 50% of LIRGs are spirals above z $\sim$ 0.5, declining to a third at lower redshifts (Bell et al., 2005). Additionally, LIRGs below $\sim 10^{11.5} L_\odot$ seem to be non-interacting, shifting to interacting or merging above. Many of the LIRGs also host outflows in dif-

ferent ways. Winds are often driven by starburst in the central region, while collimated jets are primarily driven by AGNs. These connect the nuclei to the host galaxy and exert feedback on it, quenching starformation and perhaps regulating the growth of the SMBH. The outflows seem to be multiphase with most of the ISM mass being expelled through cold gas outflows.

The outflows have been detected in different wavelength regimes, with the *Herschel* Space Telescope detecting 500-1500 km/s winds primarily in 119 μm OH lines over wide angles (e.g., Sturm et al., 2011), ALMA detections of molecular mm/sub-mm CO in outflows (e.g., Aalto, Muller, Sakamoto, et al., 2012) and also molecules such as HCN and HCO^+, indicating the harsh environment due to their high excitation temperatures requirements (e.g., Aalto, Garcia-Burillo, et al., 2015). While radio-jets are a common power source for molecular outflows, some LIRGs also host collimated radio-quiet molecular jets, the physics of these jets still remain unclear (e.g., Falstad et al., 2017).

2.5 Compact obscured nuclei

Some (U)LIRGs exhibit nuclei with obscuration levels as high as $A_V \gg 1000$, which for example can be probed through silicate dust absorption features at 9.7 and 18 μm (see section 3.1 and 3.3). Extinctions of this magnitude are caused by high column densities of $N(H_2) > 10^{24}$ cm^{-2}, which hinder infrared diagnostics used to probe the nature of the central source, forcing us to observe in the far-infrared or (sub)millimeter regime. The obscuration source in these objects seem to be on the scale of tens of parsecs with gas and dust at temperatures of $T \sim 100 - 300$ K, giving these sources the name of compact obscured nuclei (CON) (Falstad et al., 2017; Falstad et al., 2017). It is uncertain whether the central power source is stellar or SMBH in nature. It might be a distinct phase of accreting SMBH or perhaps highly compact and you stellar clusters, or a combination of both (e.g., Aalto, Muller, König, et al., 2019). While radiatively excited H_2O and OH can be used as diagnostic tools for CONs with obscuring column densities up to $N(H_2) > 10^{25}$ cm^{-2}, the most compact CONs exhibits $N(H_2) \sim 10^{26}$ cm^{-2}, where these tools are unreliable. In these cases vibrationally excited HCN and other mm and sub-mm emission lines can be used in the quest of unveiling the nature of the obscured power source.

CHAPTER 3

Cosmic dust

Cosmic dust plays a fundamental role in galaxy evolution and serves as a crucial diagnostic tool for understanding the physical conditions within galaxies. In luminous infrared galaxies, dust grains absorb ultraviolet and optical radiation from stars and AGNs, reprocessing this energy into infrared emission that dominates the galaxy's spectral energy distribution. The mid-infrared spectral features arising from stochastically heated nano-grains provide unique insights into the radiation field strength, gas density, and chemical processing occurring within these extreme environments. With the unprecedented sensitivity and spectral resolution of the *James Webb* Space Telescope, we can now resolve individual emission features and subfeatures that were previously undetectable, allowing for detailed analysis of grain composition, size distribution, and the physical processes governing dust evolution in galaxy mergers. Originally studied primarily for its obscuring properties in the ISM, cosmic dust research has expanded to encompass its rich diagnostic capabilities. By mass, dust is estimated to constitute 0.5-1% of the ISM (Ferriere, 2001), yet its influence far exceeds this modest fraction. Two main categories of dust have been confirmed: carbonaceous and silicate grains, though the exact composition and size distribution remain unknown. The increased sensitivity of

infrared facilities such as *Spitzer* and *JWST* has enabled intensive research into dust's fundamental nature. Previously mysterious features such as the 2175 Å extinction bump and the unidentified infrared bands (UIR bands) have received plausible explanations, while others, such as the diffuse interstellar bands (DIBs) and the extended red emission (ERE) in the near-infrared and visible, remain enigmatic. Simultaneously, increasingly fine spectral features continue to be discovered. The observed depletion of elements such as C, O, Mg, Si, S, and Fe in the gaseous ISM suggests these are the primary building blocks of the dust population.

3.1 Dust extinction

As light from a source travels through the interstellar and intergalactic medium, it will be scattered and absorbed by dust and gas, a process known as extinction. If the obscuring medium does not emit light by itself, the observed light will be given by $I_\lambda(\tau_\lambda) = I_\lambda(0)e^{-\tau_\lambda}$, where $I_\lambda(\tau_\lambda)$ is the observed intensity after extinction, $I_\lambda(0)$ is the intrinsic (unextincted) intensity, and τ_λ is the total optical depth. The optical depth is the sum of absorption and scattering contributions: $\tau_\lambda = \tau_{\lambda,\mathrm{abs}} + \tau_{\lambda,\mathrm{sca}}$. The extinction is then given by:

$$A_\lambda = 2.5\log_{10}[I_\lambda(0)/I_\lambda(\tau_\lambda)] \approx 1.086\tau_\lambda$$

Since both intrinsic intensity and optical depth cannot be measured directly, the usual approach is to measure the color excess. The color excess is defined as $E(\lambda,\lambda') = A_\lambda - A_{\lambda'}$ and is a measure of the optical depth difference between two wavelengths. Observationally, this is measured as $E(\lambda,\lambda') = \Delta m_\lambda - \Delta m_{\lambda'}$, where m_λ is the apparent magnitude at λ. Using the B-band at $\lambda = 0.44$ μm and V-band at $\lambda = 0.55$ μm as reference wavelengths, the extinction at wavelength λ is measured by:

$$\mathrm{Ext}(\lambda) = \frac{E(\lambda,V)}{E(B,V)}$$

The extinction profile changes along different lines of sight and towards different targets (see Figure 3.1). Figure 3.1 shows a distinct peak at 2175 Å, known as the "UV extinction bump", followed by the FIR rise. Although extensive research on the origin of this extinction feature, no clear cause has

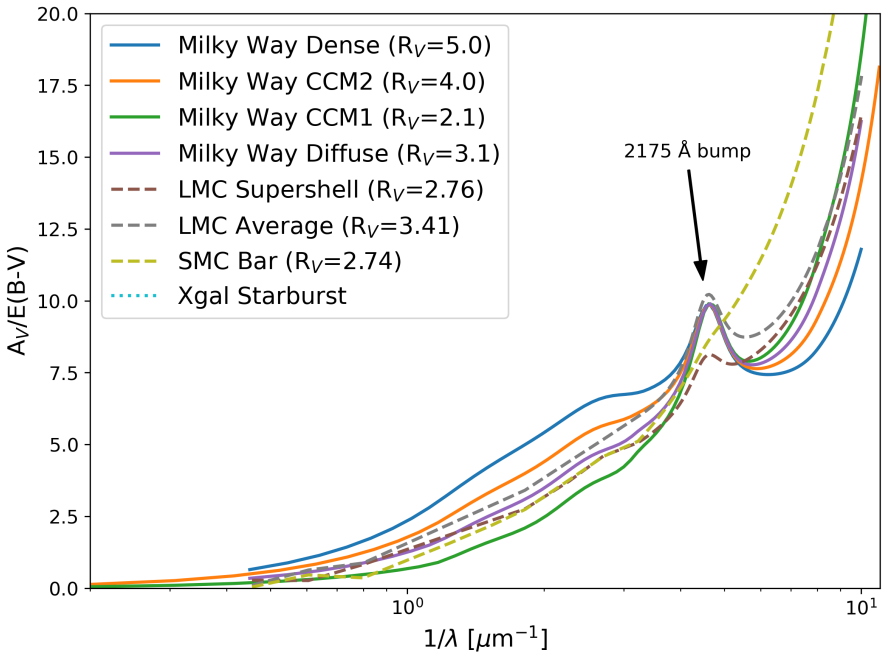

Figure 3.1: Extinction curves towards a selection of targets. Indicated slope values are the reddening values defined by $R_V = A_V/E(B,V)$. Extinction curves from Cardelli et al. (1989), Gordon et al. (2003), and Calzetti et al. (2000).

been identified. While its strength and width vary with target, central wavelength barely does. Suggested sources to the features are graphite, polycyclic aromatic hydrocarbons (PAHs), amorphous carbon, silicate grains among else.

Other features of dust extinction is absorption from carbonaceous features such as the 3.4 μm aliphatic feature (e.g., Pendleton et al., 2025), and the prominent 9.7 and 18 μm silicate features. Water ice features such as 3.1 and 6.1 μm water ice are also observed, mainly towards shielded regions (e.g., Dartois et al., 2001).

3.2 Carbonaceous grains

Large grains at thermal equilibrium

Dust grains larger than ∼30 nm are considered "large", with total energy content not changing considerably upon absorption of quanta and can be treated with classical physics. The main processes of heating and cooling involves radiative and collisional heating and radiative cooling. However, in the cold neutral medium, the fraction of collisional to radiative heating is of order 10^{-5}, and hence not important. Figure 3.2 shows the dust grain emission spectrum calculated using DustEm (Compiègne et al., 2013) based on the Themis dust model of Jones et al. (2017). When the large grains are in thermal equilibrium, the emitted radiation follows a Planck distribution with characteristic size specific grain temperatures on the order of 10-20 K. Figure 3.2 shows the temperature distribution for different grain sizes. As the grain size increases from less than a nanometer to several tens of nanometers, the distribution width decreases, clearly displaying the single temperature representation of large grains being justified.

Stochastically heated nano-grains

In the cosmic dust size distribution we also find the very small grains, also referred to as nanograins and PAHs.

These grains have low heat capacities, meaning their total internal vibrational energy is comparable to or less than the average energy of absorbed photons. When such a grain absorbs a single photon, its temperature can increase dramatically and fluctuate randomly over time, a process known as stochastic heating. It is no longer possible to characterize all grains of a spe-

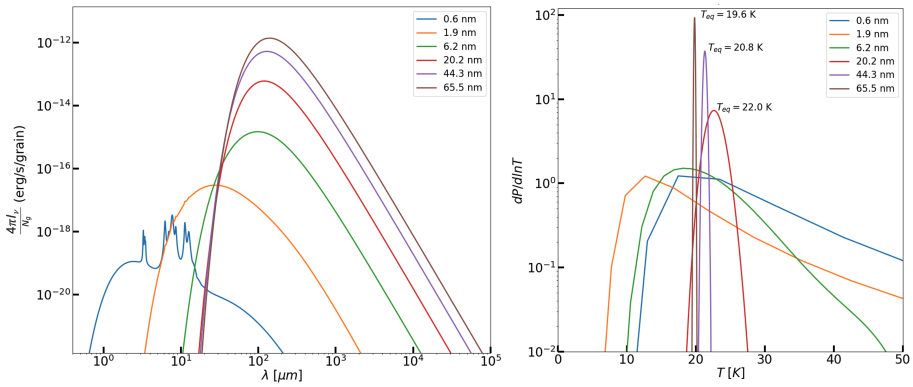

Figure 3.2: *(Left)* Dust grain emission spectrum calculated using DustEm (Compiègne et al., 2013) based on the Themis dust model of Jones et al. (2017). *(Right)* Dust grain temperature distributions calculated using DustEm (Compiègne et al., 2013) based on the Themis dust model of Jones et al. (2017).

cific size with a single temperature, instead the width of the distribution is substantial (see Figure 3.2). These grains have significantly low heat capacities, causing absorption of photons to produce dramatic temperature spikes (see Figure 3.3). While absorption of quanta for large grains with comparably high heat capacity and cross sections will result in steady temperature at thermal equilibrium, a decrease in grain size will result in absorption being less frequent but lead to higher temperature spikes. The incidence of the spikes over time will depend on radiation field intensity, meaning a strong radiation field is expected to produce more temperature spikes, and therefore grain excitations. The nanograins will on excitation release the energy in specific energy bands corresponding to the excitation level and the SED of a size specific population will begin to show the emission bands on top of the Planck profile (see Figure 3.2). The emission bands of such a size specific population of nanograins are found in Figure 3.3.

The origin of the stochastically heated grain emission bands were long unknown and were hence named unidentified infrared bands (UIR bands). These were later identified to originate from aromatic rich hydrocarbonaceous grains and PAHs (Duley et al., 1981; Leger et al., 1979; Allamandola et al., 1985). Aromatic rich grains consists of benzene ring-structured carbon skeletons with

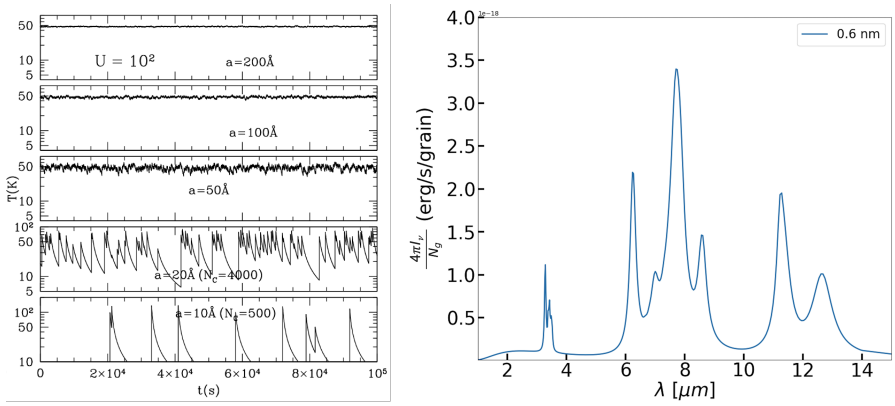

Figure 3.3: *(Left)* Temperature change over time for different dust grain sizes on absorbing quanta. Figure from Draine (2011). *(Right)* Example SED for stochastically heated nanograins with aromatic and aliphatic rich band. SED produced using DustEm (Compiègne et al., 2013).

hydrogen atoms on the perimeter and emit mainly in bands centered around 3.3, 6.2, 7.7, 8.6, 11.3 and 12.7 μm (see Figure 3.3). Excitation modes includes stretching of the hydrogen-carbon bonds and in and out of plane bending of the same as well as vibration of the carbon skeleton.

In addition to the aromatic emission features, aliphatic structures within the grains also produce emission bands (Duley et al., 1983). Aliphatic structures are open chains of carbon with hydrogen atoms attached, giving these structures a higher hydrogen to carbon ratio as compared to the aromatic structures. Features arising from excitations of aliphatic compounds in the grains include the 3.4 μm complex (Jourdain de Muizon et al., 1990) as well as the 6.9 and 7.3 μm features (Kwok et al., 1999). Most of the carbonaceous features from stochastically heated grains are thought to consist of multiple subfeatures. The aliphatic 3.4 μm complex consists of multiple subfeatures. Boutéraon et al., 2019 reporting five in protoplanetary discs, centered around 3.4, 3.43, 3.46, 3.52 and 3.56 μm (see Figure 3.4). Chown et al., 2024 detected up to six subfeatures towards the Orion Bar centered at 3.395, 3.403, 3.465, 3.516 and 3.561 μm. They also found a vast number of subfeatures across all carbonaceous features using JWST. Disentangling and identifying these subfeatures is a subject of intense research and the topic is explored further

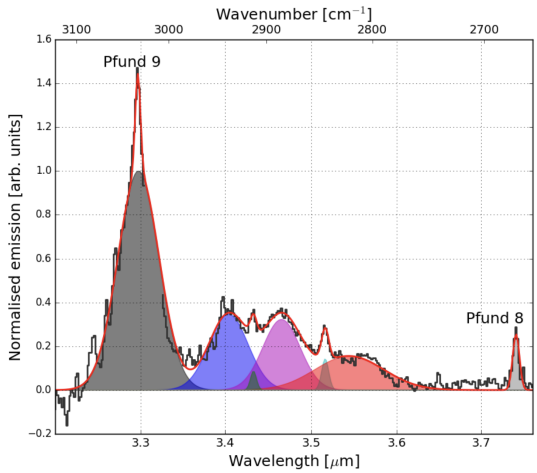

Figure 3.4: Spectral decomposition showing the aromatic 3.3 μm feature and the aliphatic 3.4 μm complex with subfeatures centered at 3.4, 3.43, 3.46, 3.52, and 3.56 μm. Figure from Boutéraon et al., 2019.

in the included paper.

3.3 Silicate dust

Also found in the cosmic dust population are the silicate dust grains. The composition of the silicate grains are not fully understood, but main features of the silicate type dust are the 9.7 and 18 μm features, arising due to Si-O stretching and O-Si-O bending respectively. These are often observed in absorption, with the 9.7 μm feature sometimes extending up to 2 μm (e.g., Kemper et al., 2004). Silicate dust exists primarily in amorphous and crystalline states. Observations suggest that $\lesssim$2.2% of the silicate population is crystalline (Kemper et al., 2005).

3.4 Dust processing

Dust grains are expected to vary with the environment in which they are found. Processes such as coagulation, fragmentation, accretion and evapo-

ration are all expected to affect the spectral signatures of dust in our Universe. Changes in physical conditions alter the composition, size, and shape of dust grains, which in turn affects their mid-infrared spectral features. These changes in carbonaceous features have been linked to variations in PAH abundance (e.g., Peeters, Hony, et al., 2002; Peeters, Mattioda, et al., 2004). Studies by e.g., Abergel et al., 2002, Rapacioli et al., 2005 and Berné et al., 2007 provided evidence that PAH photodestruction in photodominated regions (PDRs) could be responsible for the mid-infrared variations observed in these environments. Studies have also found that correlated features can still have a varying relative strength depending on radiation field. Galliano et al., 2008 observed variations in the relative strengths of the aromatic 6.2, 7.7, and 8.6 μm features compared to the 11.3 μm feature, which they attributed to changes in the abundance of ionized PAHs due to UV photoprocessing. Pilleri et al., 2015 found a linear correlation of the aliphatic 3.4 μm complex to the aromatic 3.3 μm feature with the radiation field strength as probed by the [NeIII]/[NeII] ratio, with the aliphatic abundance decreasing with increasing neon ratio. It has been explained through a more efficient destruction of the weaker aliphatic C-H bonds as compared to the stronger aromatic bonds, leading to an aromatization of the grain population. However, Boutéraon et al., 2019 found a flat relationship between these ratios in the proto-planetary discs of Herbig stars. They attributed this to a constant replenishment of small grains on the disc surface, provided by destruction of large aliphatic rich grains. Studies such as Carrasco et al., 1973; Jura, 1980; Cardelli et al., 1989 have also suggested high density regions such as dark clouds promotes grain growth, either through coagulation or heavy element depletion onto the grain surfaces.

CHAPTER 4

Observations and data reduction

4.1 James Webb Space Telescope

Launched on 25th of December 2021 from Europe's Spaceport in French Guiana, on an Ariane 5 rocket, and fully ready for use in July 2022, the *James Webb* Space Telescope *(JWST)* is an infrared observatory operating in the wavelength range 0.6 μm to 28.5 μm (NASA, 2025). The telescope has a segmented dish of 18 hexagonal mirrors, giving a total mirror diameter of 6.5 m. JWST have four instruments available onboard:

- Mid InfraRed Instrument (MIRI), consisting of an imager (Kendrew et al., 2015; Dicken et al., 2024) and a spectrograph (Wells et al., 2015; Argyriou, Glasse, et al., 2023)
- Near-InfraRed Spectrometer (NIRSpec) (Böker et al., 2022; Jakobsen et al., 2022)
- Near-InfraRed Camera (NIRCam) (Rieke, Kelly, and Horner, 2005; Rieke, Kelly, Misselt, et al., 2023)
- Near Infrared Imager and Slitless Spectrograph (NIRISS)/Fine Guidance Sensor (FGS) (Doyon, Hutchings, et al., 2012; Doyon, Willott, et

al., 2023)

For spectral analysis purposes, the NIRSpec and MIRI instruments are of interest. NIRSpec provides spectroscopy at $0.6-5.3$ μm with the Integral Field Unit (IFU) mode available. MIRI too has options for IFU, a Low Resoultion Spectrometer (LRS) which is a part of the MIRI imager module, operating at $5-14$ μm, and the Medium Resolution Spectrometer (MIRI) at $4.9-27.9$ μm respectively.

Near InfraRed Spectrograph

The Near InfraRed Spectrograph (NIRSpec) is an instrument assembly operating in the wavelength range 0.6-5.3 μm, with a field of view (FoV) of 3" $\times$ 3" (see Figure 4.4). It serves multiple modes of observation including a Micro Shutter Assembly (MSA) for multi object spectroscopy, an Integral Field Spectroscopy (IFS) for smaller targets using Integral Field Unit (IFU) image slicing optics, and also fixed slit modes (Böker et al., 2022). Figure 4.1 shows the beam path from the telescope through the instrument. The light is directed into the NIRSpec instument via a set of mirrors, passing through a Filter Wheel Assembly (FWA) and appropriate filters (selected for different wavelength bands) followed by a refocusing mechanism (RMA). The beam falls on the Micro Shutter Assembly (MSA) and depending what mode is to be used, the light passes through different apertures of the assembly, e.g. the Integral Field Unit (IFU) aperture for full 3D-image cubes. Entering the spectrometer the beam is directed to the Grating Wheel Assembly (GWA) which disperses it in wavelengths and project the light onto the detector (two sensor chip assemblies, SCAs) (Böker et al., 2022; Jakobsen et al., 2022). Since these detectors are physically separated, there will always be loss of data, known as the NIRSpec IFU wavelength gap. In the included paper, the NIRSpec IFU-mode has been used with the filter/grating combinations F100/G140H (0.97-1.89 μm), F170/G235H (1.66-3.17 μm), F290/G395H (2.87-5.27 μm).

NIRSpec IFU is inherently undersampled. This means the point spread function (PSF) – which describes how light from a point source spreads across the detector – is sampled by too few pixels. An undersampled observation has the effects of ineaxact position capture, since information is lost at detector level. An observation is properly/critically sampled when the smallest information size, the PSF, is twice sampled. This is called Nyquist sampling and

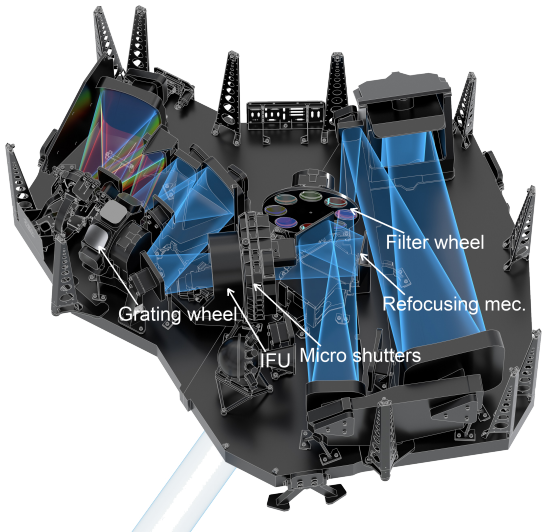

Figure 4.1: Near Infrared Spectrograph (NIRSpec) beampath showing the light path from instrument input (upper right) through various optical components to the detector (upper left). Photo: ESA/ATG medialab (*labels added by Gustav Olander*).

reads $d_{\text{pixel}} = \text{FWHM}/2$, where d_{pixel} is the pixel size required and FWHM is the full width at half maximum of the PSF. Having an undersampled PSF means the measured light from a source is highly dependent on where it falls on the detector – whether in the center of pixels or between pixels – will give different flux outputs which could lead to a skewed image. Böker et al. (2022) suggest using dithering to mitigate these effects, which involves performing multiple exposures with slightly different pointings. Through dithering followed by a drizzle technique (Fruchter et al., 2002), one can restore a properly sampled image. Multiple dithering patterns are available depending on science case. The strategy used in NIRSpec IFU observations described in the included paper, a 4-point dithering pattern, is shown in Figure 4.2.

Mid-InfraRed Instrument

The Mid-Infrared Instrument, operating in the wavelength range 4.9-27.9 μm, has four operating modes; Medium-resolution spectroscopy (MRS), Low-

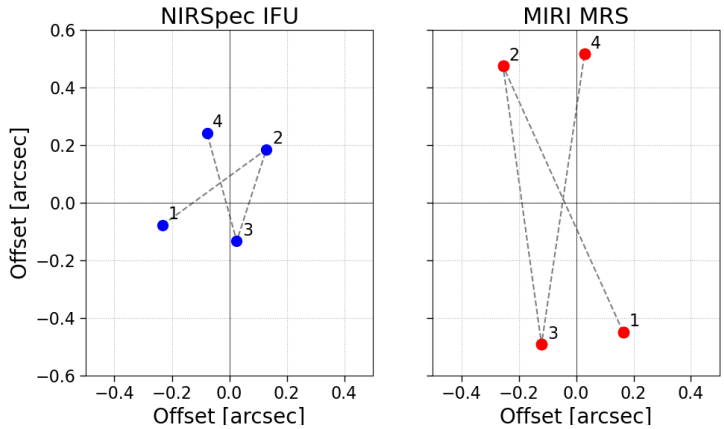

Figure 4.2: 4-point dithering pattern of *JWST* observations using NIRSpec IFU *(left)* and MIRI MRS *(right)*.

resolution spectroscopy (LRS), imaging and coronographic imaging. The mode used in the study described in the included paper is the MIRI MRS – a spectrograph that disperses the light from four IFUs (after passing through the spectrometer pre-optics, SPO), through a set of dicroic/grating wheel assemblies, onto two pairs of arsenic-doped silicon detectors (MIRIFULONG and MIRIFUSHORT) (Wells et al., 2015). The MIRI spectroscopy beam path is shown in Figure 4.3. The spectrometer has four main channels, 1 through 4, with MRS mode spectral ranges according to $4.90 - 7.65$ μm, $7.51 - 11.7$ μm, $11.55 - 17.98$ μm and $17.70 - 27.90$ μm accordingly. All are observed simultaneously with channel 1 and 2 resulting from detector MIRIFUSHORT, while channel 4 and 3 are from MIRIFULONG. By the use of dicroic/grating wheel assemblies, each channel has three subchannels; short (A), medium (B) and long (C), observed consecutively giving 12 subbands. The FoV for channel 1 through 4 are 3.2" × 3.7" to 6.6" × 7.7" (Law et al., 2023), see Figure 4.4.

MIRI MRS too is undersampled, both spatially and in the spectrally (Law et al., 2023). As a result, an advantageous observational strategy is to perform dithering, to fill the phase space of the observations to avoid aliasing. The MIRI MRS observations described in the included paper was performed with a 4-point dithering strategy (see Figure 4.2).

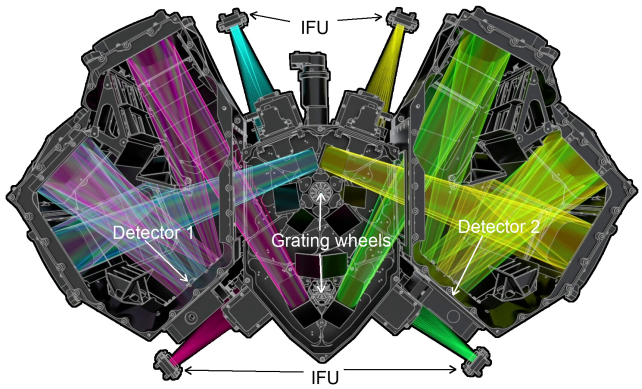

Figure 4.3: MIRI Spectroscopy beampath showing the light path from the position of the four IFUs to the two detectors, passing through grating wheels and other optics. Photo: ESA/ATG medialab (*labels added by Gustav Olander*)

Data reduction Pipeline

The JWST pipeline (Bushouse et al., 2025), described in Böker et al., 2022 and references therein for NIRSpec IFU mode, and Labiano et al., 2016 for MIRI MRS mode, consists of three stages described below.

General reference for data reduction pipeline stages:
"JWST User Documentation" (https://jwst-docs.stsci.edu)

Stage 0

Uncalibrated data is given to the observer as "*uncal.fits" files, with data in units of Data Number (DN), i.e. digitalized analog detector values. These have been produced from raw spacecraft data by Science Data Processing (SDP) system where the main header information based on the observation specifications are added. The process of producing the uncal-files are performed in stage 0 of the data reduction pipeline and is not performed by the observer. The data is the input to the observer performed data reduction pipeline, stage 1 through 3. These files are 4-dimensional containing up-the-ramp readout information, where up-the-ramp is a non-destructive de-

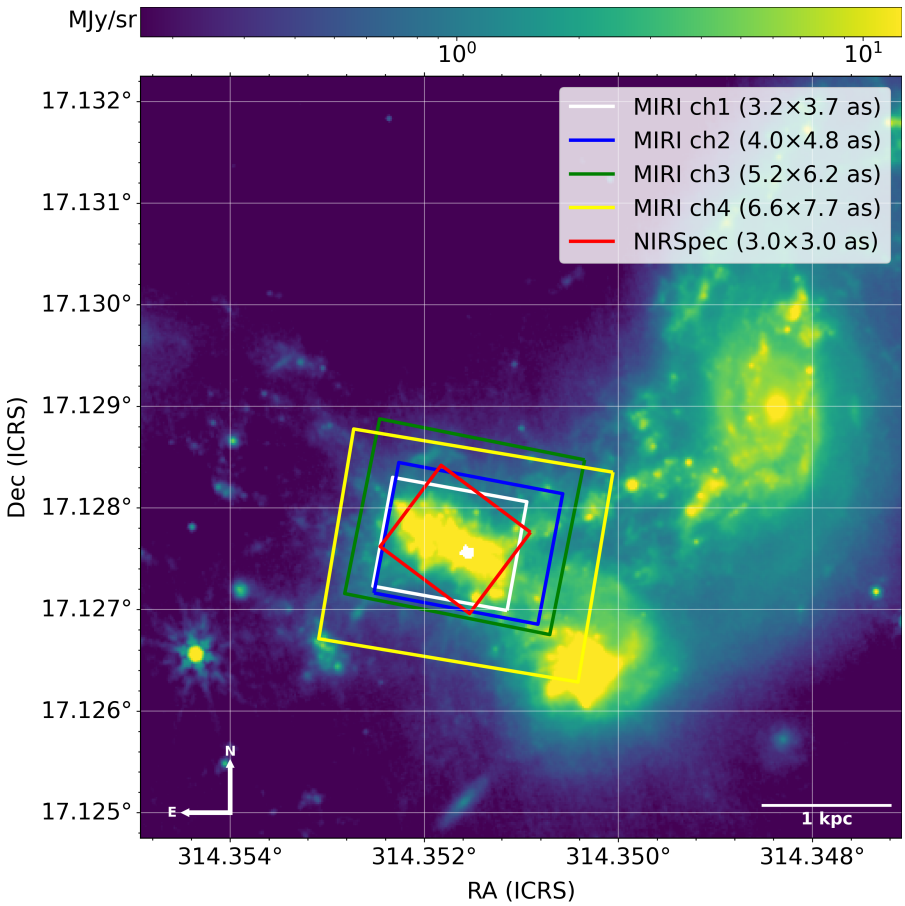

Figure 4.4: Field of view comparison showing NIRSpec IFU coverage (red) and MIRI MRS channel coverage (white, blue, green, and yellow) overlaid on a NIRCam F356W wide filter image of the merger LIRG II Zw 096.

tector value readout technique used on JWST. The 4D data contain spatial position, number of groups (a sum of detector readouts) per integration and integrations per exposure, all according to the readout pattern chosen based on observational needs selected in the Exposure Time Calculator (ETC) and Astronomers Proposal Tool (APT).

Stage 1

With uncal-files as input, the stage1, or "calwebb_detector1" pipeline is applied to all exposure types, imaging, spectroscopy etc. This stage produces count rate images ("*rate.fits") in units of DN/s per integration (or exposure) and consists of ramp-fitted images, which are detector level corrected, and integration averaged readout data. Part of pipeline stage 1 is cosmic ray detection and flagging.

Stage 2

Stage 2 differ depending on observation type. For spectroscopic data using NIRSpec IFU or MIRI MRS, the "calwebb_spec2" pipeline is applied, which fully calibrates individual exposures from countrate products from stage 1. The pipeline contains a large number of modules, each applied to specific observational setups. Whether a module is applied is controlled by the CRDS-files (JWST Calibration Reference Data System). Important steps applied to spectroscopy data in stage 2 includes assigning WCS (World Coordinate System) information to the exposures, background subtraction from background observations if available, fringe pattern correction to MIRI MRS data, flagging of MSA shutters stuck in open position for NIRSpec IFU and construction of data cubes.

Stage 3

Stage 3 of the data reduction pipeline too have different pipelines depending on observation type. For spectroscopic data the "calwebb_spec3" pipeline is implemented. Here multiple exposures are combined into single 3D data products after outlier rejection. Master background subtraction is perform if no background observation was provided in stage 2.

Fringing

MIRI suffers from dichroic fringing effects emerging as an effect of plane parallel interference in the path of the light in the detector (Argyriou, Wells, et al., 2020; Wells et al., 2015). These effects are an issue mostly in the MRS mode and present themselves as oscillations in the SEDs of spaxels in the data products. The JWST data reduction pipeline has ways to mitigate its effects to some degree by enabling the 2D-correction step "residual_fringe" in "calwebb_spec2" pipeline and the 1D-correction step "fit_residual_fringes_1d" to the extracted spectra in the finished data product. Figure 4.5 shows an example spectra before and after applying the 1D correction step.

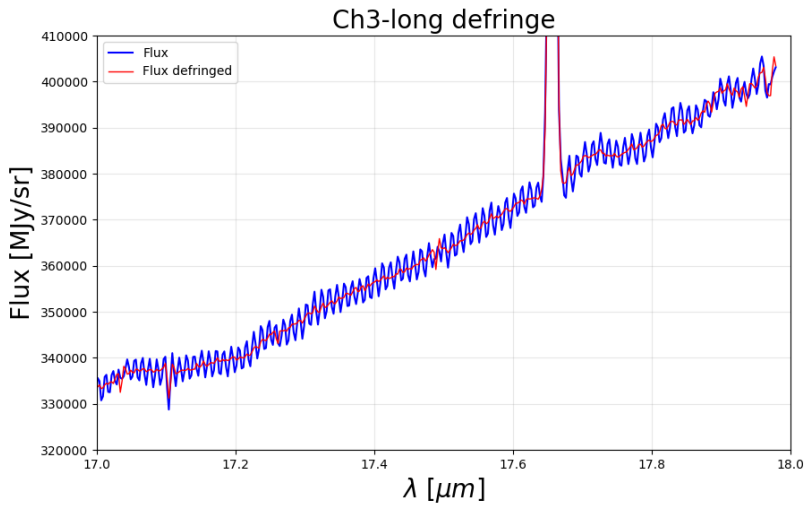

Figure 4.5: Example of calibrated data product before (blue) and after (red) applying the "fit_residual_fringes_1d" 1D correction step. The defringing was applied to a subcube box of 10x10 pixels including the continuum peak.

PSF convolution

Prior to analysis of the data products, all (sub-)channels must be convolved with the point spread function (PSF) of the detector to achieve equal resolution across the spectral axis. The PSF represents the instrument's response

to a point source, how the light propagates and spreads out over the detector and can be simulated using WebbPSF (Perrin, Soummer, et al., 2012; Perrin, Sivaramakrishnan, et al., 2014), see Figure 4.6 for an example PSF for MIRI MRS channel 3-medium at [NeIII] (15.56 μm). Since the FWHM of the PSF is dependent on wavelength, convolution of the data cubes must be done with a PSF corresponding to the longest wavelength of interest, to enable proper analysis across the spectrum. If the goal is to compare the carbonaceous features at 11.3 μm and 3.3 μm, the data cubes must all be convolved with the 11.3 μm PSF. As further described in the included paper, the data were convolved with PSFs at three different wavelengths, 3.4030 μm, 11.708 μm and 15.56 μm plus redshift of II Zw 096 at $z = 0.0361$.

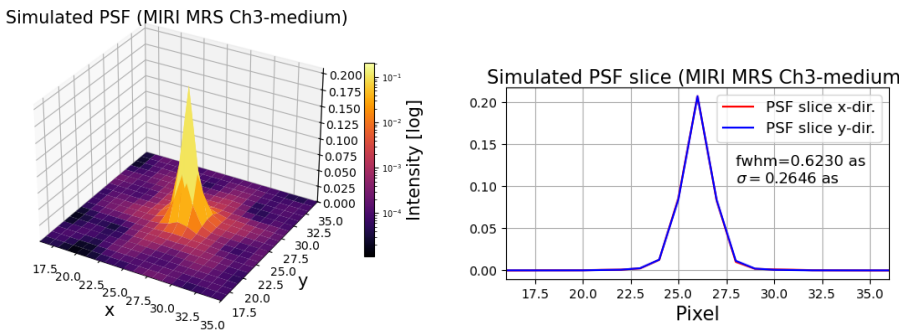

Figure 4.6: Example PSF generated using the WebbPSF tool for MIRI MRS channel 3-medium at the [NeIII] emission line (15.56 μm). *(left)* 3D image of the simulated PSF and *(right)* X (red) and Y-slices (blue) of the same PSF.

4.2 Spectral sampling

MIRI MRS is partially spectrally undersampled (Law et al., 2023), meaning that some spectral features may not be adequately resolved due to insufficient wavelength resolution. In contrast, NIRSpec is properly spectrally sampled according to the Nyquist sampling criterion, which requires $\Delta\lambda$/increment ≥ 2, where $\Delta\lambda$ is the spectral resolution element and the increment is the wavelength step between adjacent pixels. Figure 4.7 shows the spectral sampling rates for NIRSpec IFU and MIRI MRS. NIRSpec IFU operating in the

high resolution mode has nominal resolving power $R = \lambda/\Delta\lambda \simeq 2700$. The spectral axis has wavelength increments of 0.00023, 0.00040 and 0.00066 μm for the g140h-f100lp, g235h-f170lp, and g395h-f290lp channels respectively. These parameters determine the sampling rates ($\Delta\lambda$/increment) across the spectrum. Figure 4.7 also show sampling rates for MIRI MRS with increments 0.00079, 0.0013, 0.0025 and 0.006 μm for channel 1 through 4, and fits to derived in-flight values of the resolving power and the sampling rate for NIRSpec IFU and MIRI MRS.

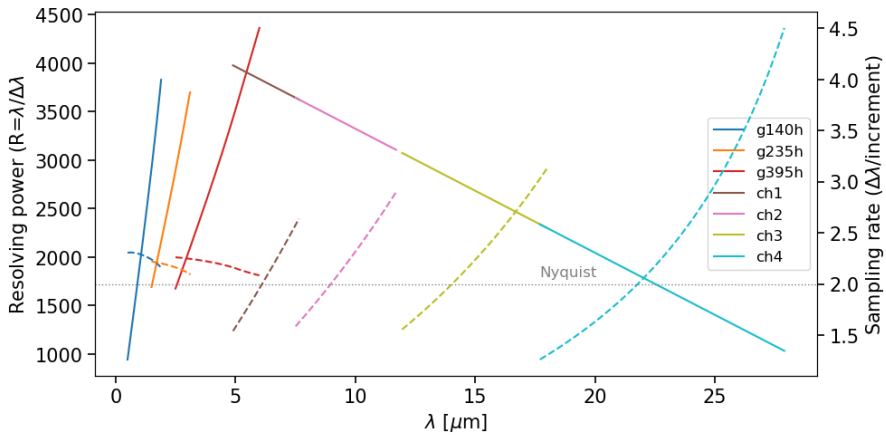

Figure 4.7: NIRSpec IFU in high resolution mode and MIRI MRS resolving power (solid lines) and spectral sampling rate (dotted lines). The MIRI MRS resolving power is a fit to in-flight derived values following $R = 4603 - 128\lambda$ from (Argyriou, Glasse, et al., 2023). Note that the sampling rate ($\Delta\lambda$/increment) does not fulfill Nyquist criterion (grey dashed line) for a substantial part of the MIRI MRS channels, meaning it is partially spectrally undersampled while NIRSpec IFU is always properly sampled.

4.3 Continuum and Feature Extraction Tool (CAFE)

To perform SED-fitting, as described in the included paper, the "Continuum and Feature Extraction tool" (CAFE) by Diaz-Santos et al., 2025 software

was used. The software is a python based programme using a least square approach to fit the SEDs extracted from the target. It is build on the work done by Marshall et al., 2007 for Spitzer Space Telescope and its InfraRed Spectrograph (IRS), expanded for JWST NIRSpec IFU and MIRI MRS data. It simultaneously fits continuum, PAH features, molecular- and atomic lines and opacity features using Levenberg–Marquardt algorithm (lmfit), least square method. The lines are fitted using Gaussian profiles while the PAH features are fitted using Drude profiles. Opacity features are fitted either through measured template spectra or through Gaussian profiles. The continuum consists of models of dust, stellar, starburst and AGN accretion disk. The dust component is modeled using five separate modified black bodies of different temperatures (cirrus, cold, cool, warm and hot), fluxes and optical depths. The AGN accretion disc, stellar and starburst components are all defined by flux and optical depth. For the latter, an age-mixing factor defining the starburst age (100MJy, 10MJy and 2MJy) is also taken into account. The user can control and change all parameters to accommodate different science cases. The tool takes calibrated observational data products as input and produces fit parameters, fitted spectra, and goodness-of-fit statistics as output.

With a calibrated data product as input, CAFE defines a grid of apertures from which a SED is extracted and fitted (see Figure 4.8). CAFE uses signal to noise (SNR) ordering method in which it first decomposes the aperture corresponding to the highest SNR, with an initial guess of parameter values defined by the user. Subsequent apertures use the resulting SED decomposition from previous ones as initial guess. Since CAFE uses a least square method, it is of high importance to define an initial guess close to a global fitting minimum, as to arrive at the most reliable solution as possible.

Updates to CAFE

Much work has focused on including new features to CAFE to ensure satisfying spectral decomposition. The following is a list of additional functionalities included in CAFE:

- **Rotation of aperture grid**. JWST data is rotated such that the Right Ascension (R.A.) and Declination (Dec.) are aligned with the x- and y-axis. In order to define the maximum number of apertures for a given FoV, a possibility to skew and rotate the grid was added (see

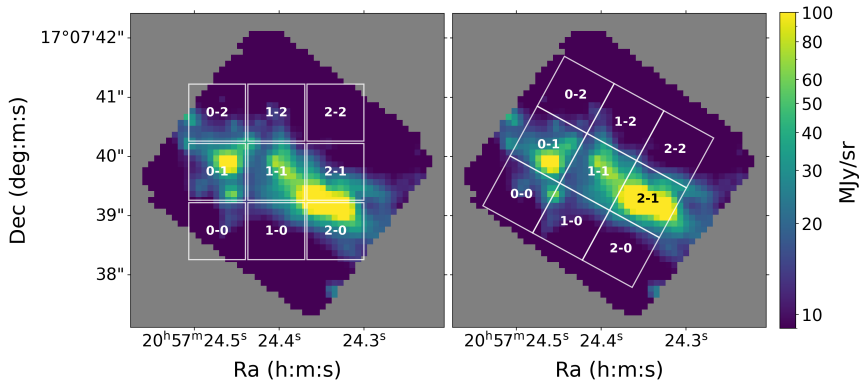

Figure 4.8: *(left)* Original way of defining an extraction grid using CAFE. *(right)* Added functionality to enable skewing of the grid and rotating of the apertures with a common angle.

Figure 4.8). By including the possibility to both skew the grid in x- and y-directions, as well as rotate apertures in the grid to a common angle, much more of the FoV could be included.

- **Negative fluxes clipping**. CAFE stiches data of different (sub-)channels and instruments to ensure no flux offsets are present, using the MIRI sub-channel 4-long as reference. This can result in negative pixels that need to be omitted in the spectral decomposition. Such a functionality was included with a possibility to remove neighboring pixels immediate surrounding them.

- **Removal of high uncertainty data**. The JWST data reduction pipeline flag bad data. However, pixels with large uncertainties are in general not subject to flagging and can therefore cause problems in the SED fitting, as way to mitigate this a functionality omitting pixels with an uncertainty greater than a user defined limit was included.

- **NIRSpec detector offset correction**. Due to the NIRSpec IFU spectrum originates from two separate detectors, a flux offset similar to that between (sub-)channels can be present. To mitigate its effects, possibly originating from flicker noise (1/f noise), focused data reduction can be performed. Residual offset correction functionality was added to CAFE

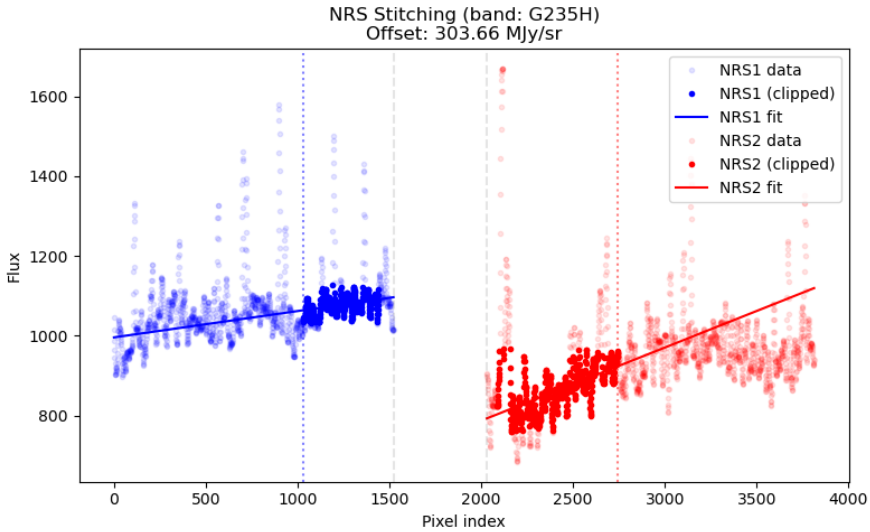

Figure 4.9: Linear fit to the end of NIRSpec IFU detector NRS1 data (blue) and start of NRS2 data (red) to determine and correct the flux offset. Solid data points are included in the fit while shaded points are excluded from the fitting and offset correction.

to further mitigate its effects. This is done through additive offset correction, which was calculated through a linear fit to sigma-clipped data points close to the wavelength gap, excluding a buffer zone in the immediate vicinity of it (see Figure 4.9).

- **Sigma clipping**. As a strategy to remove outlier pixels missed by the data reduction pipeline, and other areas of use (see "Stage execution" below), a sigma clipping functionality was added. This function uses two separate sigma levels to increase agility: an upper level for emission features and a lower level for absorption features. These values are defined by the user and omits pixels outside this range.

- **Spectral smoothing**. To ensure proper comparison between spectral features of different wavelengths, a smoothing functionality was added to achieve a common spectral resolution. This is applied to channels up to a user defined sub-channel.

- **Stage-execution**. Since science cases can vary substantially and SED profiles can differ withing the same FoV, a robust way of defining initial guesses for the decomposition is of high importance. Therefore, a new way of executing CAFE was implemented as a wrapper to the current version of CAFE that tailor the initial guesses to each aperture in the defined grid. This is accomplished by executing CAFE in three consecutive stages. Figure 4.10 presents a flowchart illustrating the data flow between these different stages. The first stage only fit the continuum components and opacity features to reach within the vicinity of the correct continuum (Figure 4.11a). In the second stage, now using stage 1 results as input, the broad PAH features are included while still allowing the continuum and opacity to vary. If successful, the output is very close to the full spectrum, only missing emission lines (Figure 4.11b). In the last stage, the result from stage 2 is used as input and all components are included and allowed to vary (Figure 4.11c). The user can also tailor what features to include in each stage and also perform single stage execution. If a previous execution up to a certain stage exists, subsequent stages can be applied using previous result as input, improving the agility of the spectral decomposition process.

- **Parallelization**. As an effect of isolating each aperture in the defined grid through the use of stage execution, CAFE can be parallelized to execute multiple regions simultaneously, vastly improving computational time (Figure 4.10)

- **Focused figures and statistics evolution**. To increase data and result visualization and goodness-of-fit presentation, functionality for plots of narrower spectral range were included (see Figure 4.11d). The user can define three areas of interest to further inspect the results. Additionally, functionality for plotting the evolution of the global fit chi-square error through CAFE iteration has been added.

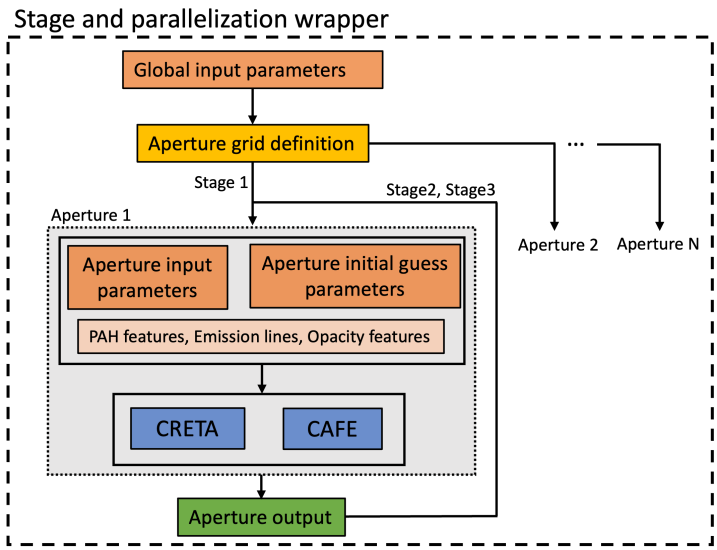

Figure 4.10: Data flow chart for stage execution and parallelization of CAFE.

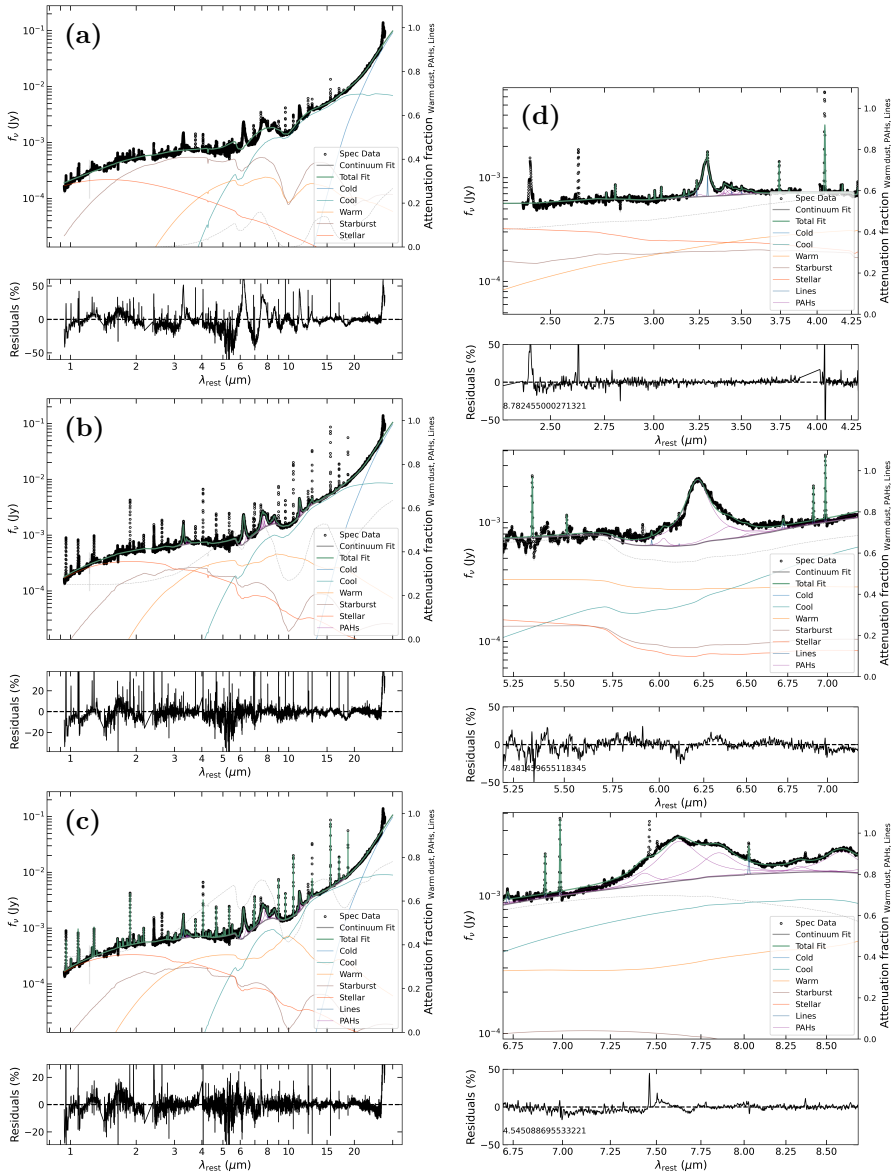

Figure 4.11: *Left*: SED decomposition outputs from CAFE from stage 1, 2 and 3. (a) Stage 1 including continuum components (in this instance also opacity features). (b) Stage 2 including continuum components, PAH and opacity features. (c) Stage 3 including all components in the SED decomposition. *Right*: Focus figures to further inspect the goodness of fit.

CHAPTER 5

Summary of the included paper

5.1 Introduction

This paper aim to map the properties of stochastically heated nanograins and find possible correlations between observed variations in properties across the nearby merger II Zw 096 and place the findings in the context of highly dynamic and dusty objects. II Zw 096 is a LIRG at a distance of 155 Mpc (redshift $z = 0.0361$) and was studied using *JWST* spectroscopic observations. LIRGs provide outstanding laboratories for study dust evolution due to their dynamics driving intense radiation environments that alter dust properties.

II Zw 096 was first studied in detail by Goldader et al. (1997) who identified four main regions, of which two being spirals (regions A and B) and two in the central region (C and D) of the system. The latter have high levels obscuration and starburst and are substantially affected by the merger. A fifth region (E) of extended and diffuse emission was also identified by Goldader et al. (1997) and later attributed to be a third galaxy by Riesco et al. (2025). Using *JWST*, Inami et al. (2022) identified clumps of high IR emission within regions C and D, indicating intense starburst. Of particular interest is a small clump responsible for 40-70 % of the system's mid-IR emission with estimated size

no larger than 175 pc. While e.g. García-Bernete et al. (2024) and Riesco et al. (2025) argues for an obscured AGN, its nature is still uncertain.

The paper describes *JWST* NIRSpec IFU and MIRI MRS observations with a FoV covering much of region C and D (see Figure 4.4). The paper covers data reduction, spectral energy distribution extraction and spectral decomposition of continuum, carbonaceous features, emission lines and opacity features.

5.2 Result

The spectral range of NIRSpec IFU and MIRI MRS cover a vast number of features from stochastically heated nanograins and emission lines. The carbonaceous features detected in II Zw 096 were the 3.3, 3.4, 6.2, 7.7, 8.6, 11.3 and 12.7 μm complexes (see Figure 5.1). Main dust features studied were the aromatic 3.3 μm, aliphatic 3.4 μm, and aromatic 11.3 μm complexes. To achieve the highest possible spatial resolution while staying clear of the undersampling effects of MIRI MRS, three grids of different sizes were defined – 3×3, 4×3 and 10×8, with aperture sizes 0.9605", 0.7874" and 0.281" respectively, depending on features to be studied.

Large variations in the integrated flux ratios of 11.3/3.3 μm across the FoV was found using the low resolution grid. Elevated ratios were found towards extreme environments such as the proposed AGN and starburst regions (see Figure 5.2), indicating larger average grain sizes in these locations, this morphology was also found in the medium resolution grid. A variation, however with a smaller dynamical range, of the 3.4/3.3 μm ratio was also found (see Figure 5.2), with lower values towards the extreme environments, indicating more effective destruction of the aliphatic compounds in these regions. The high resolution grid further identifies the lower ratios of 3.4/3.3 μm to originate from the proposed AGN and starburst regions, though the observations still not being in the spatially resolved limit and average emission from different structures. No correlation of the carbonaceous feature ratios with radiation field strength probed by the ratio of [NeIII]/[NeII] could be established.

These results further indicate dust evolution in nearby galaxies and how the physical environment affect dust properties such as grain size and composition. However, these results also demonstrates the need for spatially resolved observations in order to properly untangle the nature of dust in our Universe.

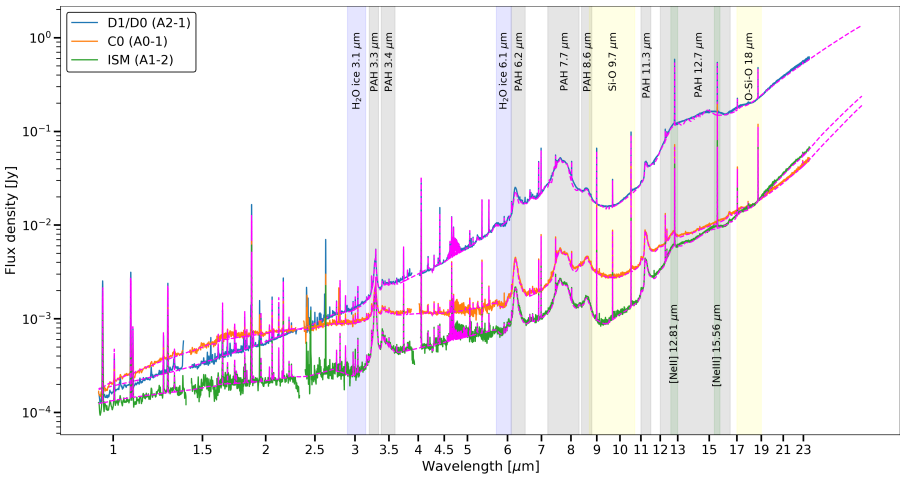

Figure 5.1: SED extractions towards three apertures in II Zw 096 targeting the proposed AGN (D1/D0) in green, starburst clump (C0) in orange, and an ISM aperture in green. Magenta indicates CAFE model fits to observed data.

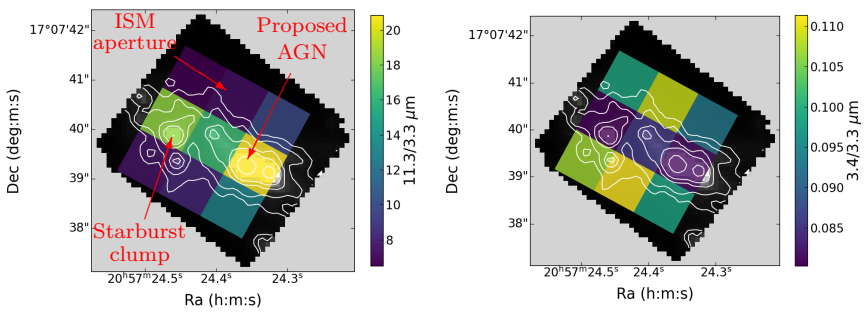

Figure 5.2: *(Left)* Integrated flux ratio map of carbonaceous features 11.3/3.3 μm. *(Right)* Ratio map of features 3.4/3.3 μm. Contours correspond to aromatic 3.3 μm feature flux.

CHAPTER 6

Concluding Remarks and Future work

This thesis has given a brief introduction to the dust and gas-obscured galaxies as well as description of dust in our Universe. Special emphasis has been put on the stochastically heated nanograins, or polycyclic aromatic hydrocarbons, giving rise to the mid-infrared carbonaceous features which can be observed using James Webb Space Telescope (JWST). In the thesis, JWST has been described in terms of its workings and how the data reduction is performed. Additionally, the usage and new functionalities implemented in the Continuum And Feature Extraction tool (CAFE) used for spectral decomposition and analysis have been described. The included paper found new implications of dust processing in galaxies outside the Milky Way and reinforced the need for much more research to fully capture the physics and processes that govern dust evolution in our Universe.

Much is still to learn about cosmic dust, how it is created, how it is destroyed and how it grows. What processes control the dust population in terms of size distribution and composition of the dust grain population? To answer these questions more research is needed. Improving models and mapping properties across multiple environments are of high importance. To further our understanding, the following possible paths are of interest for future work:

- To account for attenuation along the line of sight, extinction models are assumed. An interesting and possibly important approach to find reliable intrinsic feature fluxes could be to use different extinction models for different lines of sight. E.g. depending on dust grain sizes in different apertures of spectral energy distribution (SED) extraction, different such models could be used. For each aperture it is reasonable to expect different extinction curves, and taking this into account could lead to an improvement in results and possibly some new conclusions.

- Mapping dust properties across many different environments is of high importance to further our understanding of cosmic dust. The included paper in this thesis focus on dust in a luminous infrared galaxy. However, studying dust in the most obscured nuclei, the Compact Obscured Nuclei (CONs), could present new insights on how dust evolves in the most extreme environments in our Universe.

- JWST has the ability to map the mid infrared features from the smallest grains in the nearby Universe. It is expected that grains go through processes of fragmentation and coagulation, both growing and getting destroyed. As the grain sizes change, the spectral signatures do too. With the help of longer wavelength observatories such as ALMA, we could investigate correlations and possible causalities between dust of different sizes. Perhaps there is also a possibility to observe the remnants of destroyed grains, i.e. hydrocarbonates with emission lines occasionally present in the ALMA spectral range.

- Performing SED extraction is a computationally heavy, with several 100 free parameters sometimes to be optimized. The necessity of high-quality tools preforming these tasks is therefore clear. As part of this thesis, the spectral decomposition tool CAFE has been described, and like all tools of this kind, it too can be further improved. By doing so, e.g. through implementation of new observational and simulation results, or by more efficient and agile usage and code-base, more reliable results can be achieved.

References

Aalto, S., Garcia-Burillo, S., et al. (2015). *A&A* 574, A85.

Aalto, S., Muller, S., König, S., et al. (2019). *A&A* 627, A147.

Aalto, S., Muller, S., Sakamoto, K., et al. (2012). *A&A* 546, A68.

Abergel, A. et al. (2002). *A&A* 389, pp. 239–251.

Aghanim, N. et al. (2018). *Planck 2018 results. VI. Cosmological parameters*.

Allamandola, L. J., Tielens, A. G. G. M., and Barker, J. R. (1985). *ApJ* 290, pp. L25–L28.

Argyriou, Ioannis, Glasse, Alistair, et al. (2023). *JWST MIRI flight performance: The Medium-Resolution Spectrometer*.

Argyriou, Ioannis, Wells, Martyn, et al. (2020). *A&A* 641, A150.

Bakes, E. L. O. and Tielens, A. G. G. M. (1994). *ApJ* 427, p. 822.

Bell, Eric F. et al. (2005). *ApJ* 625.1, pp. 23–36.

Berné, O. et al. (2007). *A&A* 469, pp. 575–586.

Binney, James and Tremaine, Scott (2008). *Galactic Dynamics: Second Edition*.

Böker, T. et al. (2022). *A&A* 661, A82.

Boutéraon, T. et al. (2019). *A&A* 623, A135.

Bron, Emeric, Bourlot, Jacques Le, and Petit, Franck Le (2014). *A&A* 569, A100.

Brooks, A. M. et al. (2009). *ApJ* 694.1, pp. 396–410.

Burke, J. R. and Hollenbach, D. J. (1983). *ApJ* 265, pp. 223–234.

Bushouse, Howard et al. (2025). *Zenodo*.

Calzetti, Daniela et al. (2000). *ApJ* 533, pp. 682–695.

Cardelli, Jason A., Clayton, Geoffrey C., and Mathis, John S. (1989). *ApJ* 345, p. 245.
Carrasco, L., Strom, S. E., and Strom, K. M. (1973). *ApJ* 182, p. 95.
Choudhuri, Arnab Rai (2010). *Astrophysics for Physicists*.
Chown, Ryan et al. (2024). *A&A* 685, A75.
Compiègne, M. et al. (2011). *A&A* 525, A103.
– (2013). *Astrophysics Source Code Library*, ascl:1307.001.
Dartois, E. and d'Hendecourt, L. (2001). *A&A* 365.2, pp. 144–156.
Diaz-Santos, Tanio et al. (2025). *Astrophysics Source Code Library*, ascl:2501.001.
Dicken, Dan et al. (2024). *A&A* 689, A5.
Doyon, René, Hutchings, John B., et al. (2012). *Space Telescopes and Instrumentation 2012: Optical, Infrared, and Millimeter Wave* 8442, 84422R.
Doyon, René, Willott, Chris J., et al. (2023). *PASP* 135, p. 098001.
Draine, B. T. (2003). *ARAA* 41.1, pp. 241–289.
– (2011). *Physics of the Interstellar and Intergalactic Medium*. 1st ed. Princeton Series in Astrophysics Series v.19. Princeton: Princeton University Press. ISBN: 978-0-691-12213-7 978-1-4008-3908-7.
Duley, W. W. and Williams, D. A. (1981). *MNRAS* 196.2, pp. 269–274.
– (1983). *MNRAS* 205.1, 67P–70P.
Falstad, N. et al. (2017). *A&A* 597, A105.
Ferriere, Katia M. (2001). *RvMP* 73.4, pp. 1031–1066.
Fruchter, A. S. and Hook, R. N. (2002). *PASP* 114, pp. 144–152.
Galliano, Frédéric et al. (2008). *ApJ* 679, pp. 310–345.
García-Bernete, I. et al. (2024). *A&A* 682, p. L5.
Goldader, Jeffrey D. et al. (1997). *AJ* 113, p. 1569.
Gordon, K. D. et al. (2003). *ApJ* 594, pp. 279–293.
Herschel, William (1785). *Philosophical Transactions of the Royal Society of London Series I* 75, pp. 213–266.
Hinshaw, G. et al. (2012). *Nine-Year Wilkinson Microwave Anisotropy Probe (WMAP) Observations: Cosmological Parameter Results*.
Hollenbach, David and Salpeter, E. E. (1971). *ApJ* 163, p. 155.
Hubble, E. P. (1925). *Popular Astronomy* 33, pp. 252–255.
Inami, Hanae et al. (2022). *ApJL* 940.1, p. L6.
Jakobsen, P. et al. (2022). *A&A* 661, A80.
Jones, A. P. et al. (2017). *A&A* 602, A46.

Jourdain de Muizon, M., D'Hendecourt, L. B., and Geballe, T. R. (1990). *A&A* 235, p. 367.

Jura, M. (1980). *ApJ* 235, pp. 63–65.

Kapteyn, J. C. (1922). *ApJ* 55, p. 302.

Kapteyn, J. C. and Rhijn, P. J. van (1920). *ApJ* 52, p. 23.

Kemper, F., Vriend, W. J., and Tielens, A. G. G. M. (2004). *ApJ* 609, pp. 826–837.

– (2005). *ApJ* 633.1, p. 534.

Kendrew, Sarah et al. (2015). *PASP* 127.953, p. 623.

Keres, Dusan et al. (2004). *How Do Galaxies Get Their Gas?*

Kwok, Sun, Volk, Kevin, and Hrivnak, Bruce J. (1999). *A&A* 350, pp. L35–L38.

Labiano, A. et al. (2016). "The MIRI Medium Resolution Spectrometer calibration pipeline". *Observatory Operations: Strategies, Processes, and Systems VI*, p. 117.

Law, David R. et al. (2023). *AJ* 166, p. 45.

Leger, A. et al. (1979). *A&A* 79, pp. 256–259.

Magnelli, B., Elbaz, D., Chary, R. R., Dickinson, M., Borgne, D. Le, et al. (2009). *A&A* 496.1, pp. 57–75.

Magnelli, B., Elbaz, D., Chary, R. R., Dickinson, M., Le Borgne, D., et al. (2011). *A&A* 528, A35.

Marshall, J. A. et al. (2007). *ApJ* 670.1, pp. 129–155.

NASA (2025). *James Webb Space Telescope - NASA Science.*

NASA/ESA (1999). *The Hubble tuning fork - classification of galaxies | ESA/Hubble.*

Neugebauer, G. et al. (1984). *ApJ* 278, pp. L1–L6.

Peeters, E., Hony, S., et al. (2002). *A&A* 390, pp. 1089–1113.

Peeters, E., Mattioda, A. L., et al. (2004). *ApJ* 617, pp. L65–L68.

Pendleton, Y. J. et al. (2025). *A Tale of Two Sightlines: Comparison of Hydrocarbon Dust Absorption Bands toward Cygnus OB2-12 and the Galactic Center.*

Perrin, M. D., Sivaramakrishnan, A., et al. (2014). "Updated point spread function simulations for JWST with WebbPSF". *Space Telescopes and Instrumentation 2014: Optical, Infrared, and Millimeter Wave.* Vol. 9143. Society of Photo-Optical Instrumentation Engineers (SPIE) Conference Series. ADS Bibcode: 2014SPIE.9143E..3XP. Bellingham, p. 91433X.

Perrin, M. D., Soummer, R., et al. (2012). "Simulating point spread functions for the James Webb Space Telescope with WebbPSF". *Space Telescopes and Instrumentation 2012: Optical, Infrared, and Millimeter Wave*. Vol. 8442. Society of Photo-Optical Instrumentation Engineers (SPIE) Conference Series. Bellingham, p. 84423D.

Pilleri, P. et al. (2015). *A&A* 577, A16.

Rapacioli, M., Joblin, C., and Boissel, P. (2005). *A&A* 429, pp. 193–204.

Rieke, G. H., Lebofsky, M. J., et al. (1980). *ApJ* 238, pp. 24–40.

Rieke, Marcia J., Kelly, Douglas, and Horner, Scott (2005). *Cryogenic Optical Systems and Instruments XI* 5904, pp. 1–8.

Rieke, Marcia J., Kelly, Douglas M., Misselt, Karl, et al. (2023). *PASP* 135, p. 028001.

Riesco, Clemente et al. (2025). *AJ* 990, p. 136.

Sanders, D. B., Mazzarella, J. M., et al. (2003). *The IRAS Revised Bright Galaxy Sample (RBGS)*.

Sanders, D. B. and Mirabel, I. F. (1996). *ARAA* 34, p. 749.

Schneider, Peter (2015). *Extragalactic Astronomy and Cosmology: An Introduction*.

Shapley, Harlow (1923). *PA* 31, p. 316.

Smoot, G. F. et al. (1992). *ApJ* 396, p. L1.

Sturm, E. et al. (2011). *ApJ* 733, p. L16.

Weedman, D. W. et al. (1981). *ApJ* 248, pp. 105–112.

Weingartner, J. C. and Draine, B. T. (2001). *ApJS* 134, pp. 263–281.

Wells, Martyn et al. (2015). *PASP* 127, p. 646.

Woltjer, L. (1959). *ApJ* 130, p. 38.